Lithium intercalation in MoS_2 bilayers and implications for moiré flat bands

Zheyu Lu [1,*] Stephen Carr [2] Daniel T. Larson [2] and Efthimios Kaxiras [2,3]

[1] *Department of Physics, University of Science and Technology of China, Hefei, Anhui, 230026, China*

[2] *Department of Physics, Harvard University, Cambridge, Massachusetts 02138, USA*

[3] *John A. Paulson School of Engineering and Applied Sciences, Harvard University, Cambridge, Massachusetts 02138, USA*

(Received 25 April 2020; revised 17 August 2020; accepted 19 August 2020; published 21 September 2020)

Intercalation of lithium atoms between layers of two-dimensional (2D) materials can alter their atomic and electronic structure. We investigate effects of Li intercalation in twisted bilayers of the transition metal dichalcogenide MoS_2 through first-principles calculations, tight-binding parametrization based on the Wannier transformation, and analysis of moiré band structures through an effective continuum model. The energetic stability of different intercalation sites for Li between layers of MoS_2 are classified according to the local coordination type and the number of vertically aligned Mo atoms, suggesting that the Li atoms will cluster in certain regions of the moiré superlattice. The proximity of a Li atom has a dramatic influence on the interlayer interaction between sulfur atoms, deepening the moiré potential well and leading to better isolation of the flat bands in the energy spectrum. These results demonstrate the importance of chemical intercalation as a powerful means for controlling moiré flat-band physics in 2D semiconductors.

DOI: 10.1103/PhysRevB.102.125424

I. INTRODUCTION

Strongly correlated insulating behavior and unconventional superconductivity have recently been observed in magic-angle twisted bilayer graphene [1,2]. The small twist angle between the two graphene layers creates a moiré pattern with a characteristic length scale much greater than the lattice constant of the individual layers. The interlayer hybridization of the two layers' Dirac cones results in the emergence of flat bands in the low-energy band structure [3]. This reduction of the electrons' kinetic energy favors the usually weak electron-electron interactions and phonon-electron coupling in graphene, leading to twist-induced correlated behavior.

Flat bands and correlated physics have been predicted and observed in other moiré superlattices, such as trilayer graphene on top of hexagonal boron nitride [4,5] and twisted bilayer-bilayer graphene [6–11]. In addition, novel absorption peaks, interpreted as intralayer and interlayer moiré excitons, have been observed in different twisted bilayer transition metal dichalcogenide (TMDC) moiré superlattices due to enhanced electron-hole interactions [12–15]. Moiré flat bands were predicted to form at the band edges of twisted bilayer TMDC systems [16–19], and they have recently been observed [20]. These discoveries have demonstrated how the twist angle can be a powerful tool for engineering new and interesting properties in two-dimensional van der Waals heterostructures.

Experimental control of the twist angle can be combined with other tunable perturbations common in nanomaterial experiments. For example, vertical pressure [21–23] and external strain [24] have been investigated as additional tools to realize flat bands in a wider range of geometries and twist angles. At the same time, intercalation of Li atoms has been used to electrochemically dope the layers in van der Waals heterostructures [25,26], and has been predicted to enhance the interlayer coupling in the AA-stacked regions of twisted bilayer graphene [27]. It is worth noting that the exact details of experimental interlayer intercalation are still under investigation, even for untwisted bilayers. A complication that arises when intercalating H phase TMDCs is that a high concentration of lithium can cause a transition to the T or T' phase [28]. For experiments using edge contacts, the Li ions can cause the transition near the contacts, damaging them and preventing measurement before the ions can fully intercalate the region between the layers. In contrast to such a lateral intercalation approach, one could attempt to intercalate Li ions vertically at low concentration [29], in which case the diffusion will be slow but may drastically reduce the likelihood of a phase transition. The detailed dynamics of Li intercalation will likely be very important for the feasibility of specific experiments, but that is not our focus here. In the present work we explore the effects of lithium intercalation in various untwisted, local stacking arrangements of two layers of MoS_2, demonstrating significant amplification of the interlayer interactions caused by nearby lithium intercalants. From the calculated changes in local electronic structure, we present a continuum model for the band structure of twisted bilayer MoS_2 at small twist angles. The intercalants enhance the moiré potential, leading to better isolation of the flat bands in the energy spectrum.

The paper is organized as follows: In Sec. II we describe the density functional theory (DFT) and Wannier transformation formalism used to extract *ab initio* parameters used in our modeling. The crystal structure of twisted bilayer MoS_2 is

*Present address: Department of Physics, University of California, Berkeley, California 94720, USA.

described in Sec. III, along with our results on the energetics of Li intercalation between the layers. In Sec. IV we study the effect of Li intercalants on the interlayer coupling using both tight-binding and continuum models. We present the moiré band structure, including the effects of Li atoms, in Sec. VI. Our conclusions are presented in Sec. VII.

II. COMPUTATIONAL METHODS

DFT calculations were performed using the Vienna *ab initio* simulation package (VASP) [30,31]. The interaction between ionic cores and valence electrons is described by pseudopotentials of the projector augmented wave type. We used the SCAN meta-GGA exchange correlation functional [32], along with the rVV10 van der Waals functional [33]. We employed a slab geometry to model double layers with a 22 Å vacuum region between periodic images to minimize the interaction between slabs. The crystal structure was relaxed until Hellmann-Feynman forces were smaller in magnitude than 0.01 eV/Å for each atom. The plane-wave energy cutoff was 350 eV with a reciprocal space grid of size $17 \times 17 \times 1$ for the primitive unit cell, and grids of size $9 \times 9 \times 1$, $6 \times 6 \times 1$, and $4 \times 4 \times 1$ for the 2×2, 3×3, and 4×4 supercells, respectively. We calculated only unrotated geometries, and assessed the implications for moiré systems by sampling over different atomic registries between the layers.

To extract tight-binding parameters we transform the plane-wave DFT basis into a basis of maximally localized Wannier functions (MLWF) [34] as implemented in the WANNIER90 code [35,36]. For the Wannier transformation of bilayer MoS_2 with Li intercalants we use the seven highest valence bands and four lowest conduction bands which are composed of Mo d orbitals and S p orbitals [37]. We do not need to include the Li s orbitals because electrons from Li are primarily transferred to the surrounding layers and raise the Fermi level into the MoS_2 conduction bands, but do not form new s bands near E_F. The initial projections are chosen to be the atomic p and d orbitals and the final converged Wannier functions remain very similar to the localized atomic orbitals. The effective Hamiltonian in the Wannier basis is interpreted as the full-range *ab initio* tight-binding Hamiltonian (FTBH) [37].

In practice, MoS_2 is an n-type semiconductor [38] likely due to sulfur vacancies that form during fabrication [39]. Lithium intercalation adds electrons (negative charge carriers) and enhances the n-type doping. Thus, for prediction of transport properties we focus on the conduction band edge, which is at the K and K' points of the monolayer Brillouin zone. This band edge has very weak spin splitting in MoS_2 ($\sim$3 meV), and so we perform calculations in the absence of spin-orbit coupling. Although this choice reduces the accuracy of our electronic structure calculations, particularly around the valence K-point band edge, it greatly simplifies the tight-binding parametrization and the form of the twisted continuum model. In the discussion of our results we will address the expected effects of spin-orbit coupling.

III. ENERGETICS OF LITHIUM INTERCALATION

Each layer of MoS_2 is formed by a triangular lattice of Mo atoms sandwiched between two triangular lattices of sulfur

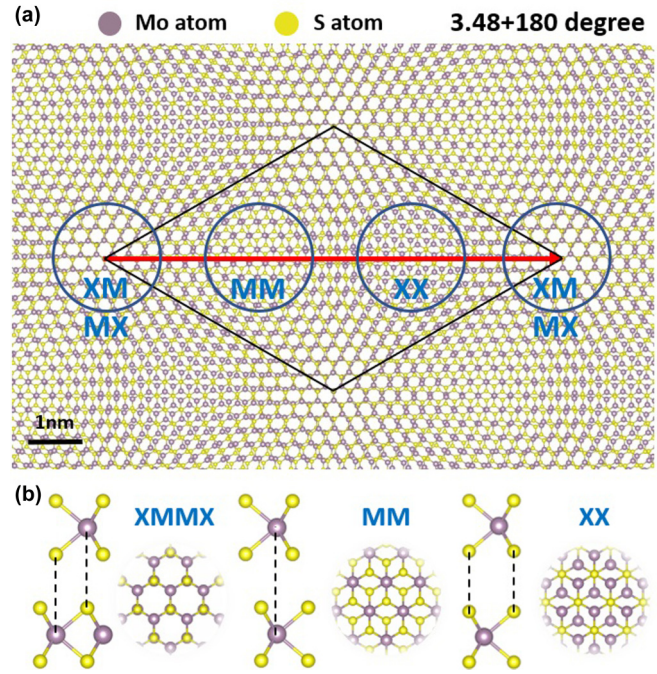

FIG. 1. (a) Top view of a twisted homobilayer of MoS_2 in the 2H phase. Different local atomic configurations occur in the small twist-angle moiré supercell. The highlighted regions correspond to local atomic configurations with threefold rotational symmetry, labeled as XMMX, MM, XX, and XMMX, respectively, along the diagonal direction. (b) Side and top views of the high-symmetry local configurations. XMMX stacking refers to the configuration with S of the top layer aligned with Mo of the bottom layer and Mo of the top layer aligned with S of the bottom layer; MM (XX) stacking region refers to the configuration where Mo (S) of the two layers are aligned.

atoms. In the naturally occurring 2H bulk phase the S atoms of each layer surround the Mo atoms with trigonal prismatic coordination, and each consecutive layer is rotated by 180° from the one below. An "aligned" bilayer can also be fabricated, where the consecutive layers have the same orientation. Here we focus on the results for a 2H bilayer; the results for the aligned case are similar. We have not studied the 1T structure, where the Mo atoms are octahedrally coordinated within each of the layers.

When one layer of a MoS_2 bilayer has a relative twist with respect to the other layer, a large scale moiré pattern forms with periodicity represented by the corresponding moiré supercell, as shown in Fig. 1(a). Within the supercell the local stacking arrangement will vary, and along the diagonal of the moiré supercell there are three special local stacking patterns with threefold rotational symmetry. In graphene these three regions are referred to as AA, AB, and BA stacking, where the "A" and "B" labels refer to the two sublattices of the honeycomb lattice. For a 2H bilayer there are more stacking possibilities, which we label by the pairs of atoms that are vertically aligned, as shown in Fig. 1(b). For a general TMDC with chemical formula MX_2 the 2H structure allows for XMMX, MM, and XX stacking. In XMMX stacking a chalcogen atom of the bottom layer is directly beneath a metal atom of the top layer, and vice versa. For MM and XX the metal atoms or chalcogen atoms are vertically aligned,

respectively. These correspond to $H_M^X = H_X^M$, H_M^M, and H_X^X, respectively, in the notation of Wu *et al.* [17]. The aligned structure allows for MMXX and MX stacking, which are equivalent to R_M^M and R_X^M in the notation of [17].

Given these different local stacking arrangements in a moiré supercell, it is important to determine the preferred locations for Li intercalants. For a single MoS_2 layer, Li adsorption occurs in the hollows of the lattice formed by S atoms, either directly above a Mo atom or an empty site in the Mo lattice. When intercalating between two MoS_2 layers a Li atom in a sulfur hollow of one layer can experience several different arrangements of sulfur atoms from the other layer, resulting in octahedral, trigonal prismatic, or tetrahedral coordination [Fig. 2(a)]. In addition to the sulfur coordination

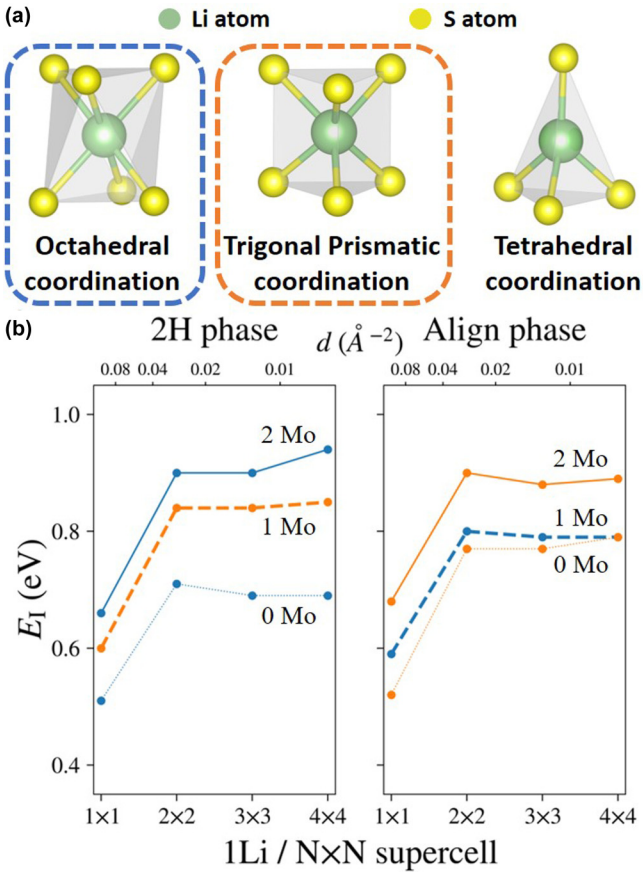

FIG. 2. (a) Atomic geometries of lithium intercalation sites with different local coordination environments: octahedral, trigonal prismatic, and tetrahedral coordination with six, six, and four S atoms symmetrically arranged around the lithium atom. (b) Li intercalation energy for both the 2*H* and aligned phases as a function of supercell size (horizontal axis); the corresponding Li concentration d is shown on the top. Each curve corresponds to a specific local coordination type and number of vertically aligned Mo atoms. Blue and orange denote octahedral and trigonal prismatic coordination, respectively. Solid, dashed, and dotted lines denote two, one, and zero vertically aligned Mo atoms. The intercalation energy does not change significantly for concentrations below one lithium per 2×2 supercell, ~ 0.03 Å^{-2}. Increasing the concentration from 0.25 Li/Mo (2×2 supercell) to 1 Li/Mo (1×1 supercell) has an energy cost of $\sim$200 meV.

of the Li atom, the number of vertically aligned Mo atoms is also important. Based on this argument, we label the possible intercalation sites by their sulfur coordination and number of vertically aligned Mo atoms. For the 2*H* bilayer there are five possibilities: octahedral-0, octahedral-2, trigonal-1, tetrahedral-0, and tetrahedral-1. The aligned case also has five intercalation sites: octahedral-1, trigonal-0, trigonal-2, tetrahedral-0, and tetrahedral-1.

The intercalation energy of lithium atoms between layers of MoS_2 is defined as follows [40]:

$$E_I = \frac{1}{n}\left(E_{MoS_2} + nE_{Li} - E_{MoS_2+nLi}\right). \quad (1)$$

Here E_{MoS_2} is the energy of the empty, relaxed bilayer of MoS_2, E_{Li} is the energy of a single Li atom in bulk bcc lithium, and E_{MoS_2+nLi} is the energy for the bilayer containing n Li atoms. E_I gives the decrease in the total energy of the system for each Li ion intercalated.

We calculate E_I for a single Li atom in a primitive cell of the bilayer, with one MoS_2 layer shifted (but not rotated) relative to the other layer, in order to produce the desired sulfur coordination and alignment with Mo. In order to understand the effect of Li-Li interactions, we repeated the calculations for a single Li atom in larger (still unrotated) bilayer supercells, which is equivalent to decreasing the Li concentration, d. For $N \times N$ supercells containing a single Li intercalant the concentration of Li is

$$d = \frac{1}{Na \times Na \times \sin\frac{\pi}{3}} = \frac{2\sqrt{3}}{3N^2a^2}, \quad (2)$$

where $a = 3.19$ Å is the primitive cell lattice constant. Figure 2(b) shows the intercalation energy for a single Li atom in each of the intercalation sites as a function of the size of the supercell. Larger supercells correspond to lower Li concentration.

For fixed Li concentration and the same number of vertically aligned Mo atoms, it is not surprising that octahedral and trigonal prismatic coordination, both with six nearest-neighbor ligands, are almost degenerate and more stable than tetrahedral coordination, which has only four nearest neighbors. The intercalation energy, and hence stability, also increases with the number of vertically aligned Mo atoms, due to a stabilizing charge transfer between the Li and Mo atoms. From Fig. 2(b) we see that for the 2*H* phase the octahedral-2 location, which corresponds to MM stacking, is the most energetically favorable, followed by the trigonal-1 location (XX stacking) and then the octahedral-0 location (XMMX stacking).

For each case, E_I rapidly reaches a plateau with increasing supercell size (decreasing Li concentration), except for tetrahedral coordination in which case the structure is not stable, possessing negative-frequency phonon modes. The energy cost to increase Li concentration from 0.25 to 1.0 Li per bilayer unit cell is $\sim$200 meV, and is caused by the repulsive nature of neighboring Li^+ ions. Because the intercalation energy does not change significantly for 2×2 and larger supercells, in subsequent calculations we will use 2×2 supercells where the Li ions are separated by $\sim$6.4 Å. Note that for Li intercalants between twisted layers of graphene the intercalation energy is sensitive to Li-Li separations up

TABLE I. Average vertical distance Δz (Å) between Mo atoms in the two layers in a 2×2 bilayer supercell with and without a Li intercalant.

	Δz (Å)	
Geometry	0 Li	1 Li
2*H* octahedral-2	6.26	6.48
2*H* octahedral-0	6.26	6.55
2*H* trigonal-1	6.85	6.90
2*H* tetrahedral-1	6.26	6.86
2*H* tetrahedral-0	6.26	7.02

to ∼15 Å [27]. But even if similar long-range interactions are present for Li atoms between MoS_2 layers, the primary contributions to the intercalation energy are captured already by the results of the 2×2 supercells. Furthermore, as will be shown below, the effect of Li atoms on the interlayer couplings are only relevant for S-S pairs within ∼3 Å of each Li atom, so sulfur pairs in the 2×2 supercell will be influenced by at most one Li atom.

The Li intercalants also modify the distances between the MoS_2 layers. Calculations with one Li atom in a 2×2 supercell indicate that Li always increases the interlayer distance, but the amount depends on its local coordination, as shown in Table I. Unsurprisingly, the tetrahedral coordination shows the largest change in the interlayer distance because there is a sulfur atom directly above the intercalant. Even in 4×4 supercells the MoS_2 layers remain nearly flat with height variations in the Mo atom of only 0.01 Å, but due to the lower effective Li concentration the layer separations are closer to the unintercalated values. To obtain accurate height profiles in a moiré system requires a twisted supercell calculation [27].

IV. EFFECT OF LITHIUM ON INTERLAYER COUPLINGS

In bilayer MoS_2 the interlayer coupling is dominated by interactions between the closest sulfur p orbitals. If there is no lithium present, such couplings have been shown to be well described by the Slater-Koster two-center approximation [37,41]. However, the introduction of Li atoms at varying distances and orientations will require additional parameters to describe accurately the interaction between S atoms in the two MoS_2 layers. We specify the location of a Li atom using polar coordinates $(r_{\mathrm{Li}}, \theta)$, where r_{Li} is the distance of the Li atom from the center of the sulfur-sulfur bond of interest, and θ is angle in the xy plane measured relative to the projection of the S-S bond, as shown in Fig. 3.

From the MLWF basis we can extract the sulfur-sulfur matrix elements as a function of Li position $(r_{\mathrm{Li}}, \theta)$. In Fig. 3(b) we plot the p_z-p_z matrix element as a function of r_{Li}, with different colors representing different values of θ. It is clear that the presence of Li can have a dramatic effect on the matrix element when Li is nearby, changing both the magnitude and even the sign. When Li is further than ∼3 Å from the center of the S-S bond, the effect is negligible. Furthermore, the orientation of the Li atom has a non-negligible but second-order effect. The other combinations of p-p matrix elements show similar behavior.

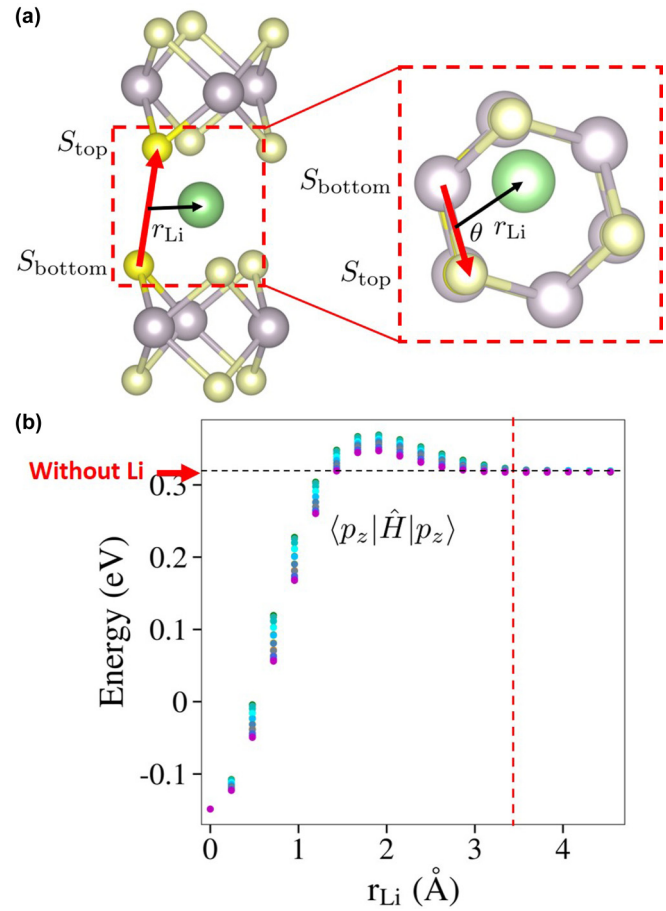

FIG. 3. (a) Diagram of the atomic sites and relevant variables for the interlayer coupling function under a three-center approximation. The red dashed box on the right provides a top-down view. The red arrow indicates the S-S bond, and the angle θ is measured from the projection of that vector into the xy plane. (b) Interlayer p_z-p_z S orbital interaction as a function of r_{Li}, with different colors corresponding to different values of θ. The black dotted horizontal line corresponds to the interaction strength without lithium. The red dotted vertical line corresponds to the range of influence of the Li intercalant.

We have analyzed how the matrix elements transform under various symmetry operations to constrain the functional form of the interlayer coupling. We considered the following operations as shown in Fig. 4:

(1) reflection in the xz plane,
(2) rotation by π about the y axis,
(3) inversion (combination of 1 and 2).

For example, consider the relation between $\langle 1_x|H_\alpha|2_y\rangle$ and $\langle 1_x|H_\gamma|2_y\rangle$, where lowercase Greek letters refer to a given Li location $(r_{\mathrm{Li}}, \theta)$. After applying an xz-plane reflection, the α configuration will transform into the γ configuration and the S atoms are mapped to themselves: $1 \to 1$, $2 \to 2$, and the p-orbitals transform as $|p_x\rangle \to |p_x\rangle$, $|p_y\rangle \to -|p_y\rangle$, and $|p_z\rangle \to |p_z\rangle$. Thus $\langle 1_x|H_\alpha|2_y\rangle = -\langle 1_x|H_\gamma|2_y\rangle$ or $t_{xy}(\theta) = -t_{xy}(-\theta)$. Following the same procedure, we can derive the transformations of the couplings under all three symmetry operations. The results are summarized in Table II.

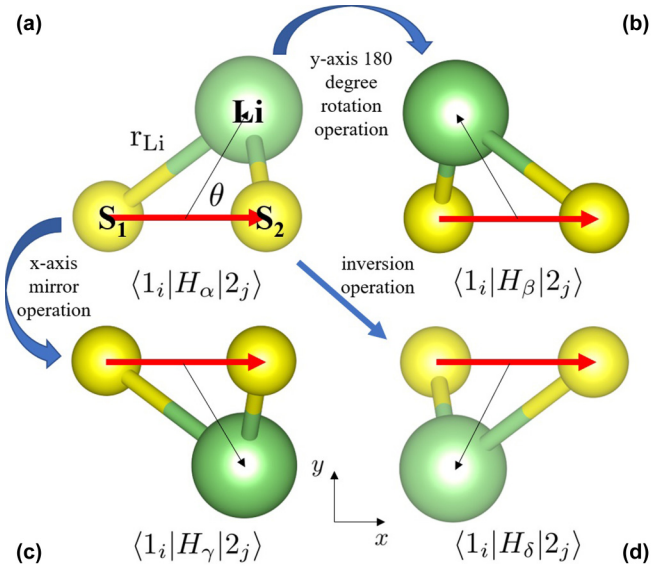

FIG. 4. Top-down view of four symmetry-related configurations under three symmetry operations. (a)–(d) α, β, γ, and δ configurations characterized by $(r_{\rm Li}, \theta)$, $(r_{\rm Li}, \pi-\theta)$, $(r_{\rm Li}, -\theta)$, and $(r_{\rm Li}, \theta-\pi)$, respectively. The left (right) yellow sphere is the sulfur atom from the bottom (top) layer labeled by 1 (2) and the green sphere denotes the lithium ion. i and j denote the atomic p orbitals p_x, p_y, and p_z. The α and β configurations are related with a rotation by π around the y axis, α and γ are related by reflection in the xz plane, and α and δ are related by inversion. The $\langle 1_i|H_k|2_j\rangle$ ($k = \{\alpha, \beta, \gamma, \delta\}$) denotes the general interlayer sulfur-sulfur p-p orbital couplings.

Based on the Slater-Koster two-center approximation for the p-p orbital interaction, we can use two functions ($V_{pp,\pi}$ and $V_{pp,\sigma}$) to describe the nine couplings. They satisfy the following relation [37]:

$$V_{pp,\pi}(\mathbf{r}) = \frac{1}{2}\sum_i t_{p_i',p_i}(\mathbf{r}) - \frac{1}{2}\sum_{i,j} t_{p_i',p_j}(\mathbf{r})\frac{r_i r_j}{r^2},$$
$$V_{pp,\sigma}(\mathbf{r}) = \sum_{i,j} t_{p_i',p_j}(\mathbf{r})\frac{r_i r_j}{r^2}, \tag{3}$$

TABLE II. Transformation of interlayer sulfur-sulfur p-p orbital couplings under reflection, rotation, and inversion. +, −, and N/A denote not changed, a sign change, and no relation after the given operation.

	xz-plane reflection	y-axis π rotation	Inversion
t_{p_x,p_x}	+	+	+
t_{p_x,p_y}	−	N/A	N/A
t_{p_x,p_z}	+	N/A	N/A
t_{p_y,p_x}	−	N/A	N/A
t_{p_y,p_y}	+	+	+
t_{p_y,p_z}	−	N/A	N/A
t_{p_z,p_x}	+	N/A	N/A
t_{p_z,p_y}	−	N/A	N/A
t_{p_z,p_z}	+	+	+

but in the presence of Li also become functions of $(r_{\rm Li}, \theta)$. Applying the results of the symmetry analysis, the two Slater-Koster functions have the following symmetries for a fixed displacement between the sulfur atoms (fixed **r**):

$$V_{pp,\sigma}(r_{\rm Li},\theta) = V_{pp,\sigma}(r_{\rm Li},-\theta) = V_{pp,\sigma}(r_{\rm Li},\pi-\theta),$$
$$V_{pp,\pi}(r_{\rm Li},\theta) = V_{pp,\pi}(r_{\rm Li},-\theta) = V_{pp,\pi}(r_{\rm Li},\pi+\theta). \tag{4}$$

Thus $V_{pp,\sigma}$ and $V_{pp,\pi}$ are completely determined for θ in the first quadrant. However, even with these constraints the form of the interlayer coupling is still highly complex. Nonetheless, the MLWF procedure captures the microscopic details of how Li affects the interlayer coupling.

V. EFFECT OF LITHIUM ON THE MOIRÉ POTENTIAL

The tight-binding approach demonstrates the dramatic influence that Li intercalants can have on interlayer couplings, but a full model accurately incorporating all the additional degrees of freedom introduced by a Li atom would be extremely complicated. To understand the effects that Li can have on the interlayer interactions in a twisted cell, we turn to a simpler continuum model for twisted bilayer TMDCs [16,17]. For the unintercalated band structure we have confirmed that the results of the continuum approximation agree well with those from a realistic tight-binding model. In contrast to the empirical form of interlayer interactions that have been used to study bilayer graphene [3], here we use *ab initio* calculations to accurately obtain the interlayer moiré potential by careful study of the DFT band structure [42]. In this case we will focus on the twisted $2H$-bilayer MoS_2.

Because Li intercalation raises the Fermi level into the conduction bands of MoS_2, we will construct a continuum model for the electronic states near the conduction band edge which can be described using the effective mass approximation. The two lowest parabolic conduction bands at the K point are a pair of identical bands from each TMDC layer, with an energy splitting caused by interlayer hybridization. Note that for the $2H$ orientation, the K point of the bottom layer corresponds to the K' point of the top layer. However, since we can safely ignore spin at the conduction K points, K and K' give identical band edges. For a twisted bilayer, a simple but robust model is comprised of two monolayer bands with effective mass m^* and an interlayer coupling $V(\boldsymbol{r})$, which is taken to be a smooth function of the position in the moiré supercell:

$$H_{\boldsymbol{k}} = \begin{pmatrix} -\frac{\hbar \boldsymbol{k}_1^2}{2m^*} & V(\boldsymbol{r}) \\ V^\dagger(\boldsymbol{r}) & -\frac{\hbar \boldsymbol{k}_2^2}{2m^*} \end{pmatrix}, \tag{5}$$

where $\boldsymbol{k}_1$ ($\boldsymbol{k}_2$) is the momentum taken relative to the K (K') point of the bottom (top) layer. A more careful consideration of the problem also takes into account a stacking-dependent on-site energy for both monolayer bands [17]. More specifically, this captures not just the band splittings but also the bands' average energy. In contrast to the explicit interlayer coupling $V(\boldsymbol{r})$, this on-site term represents changes to the in-plane electronic structure due to the presence of the neighboring layer, and so also depends on the stacking. Here we ignore this contribution, since our focus is on how lithium intercalation modifies interlayer hybridization to facilitate the

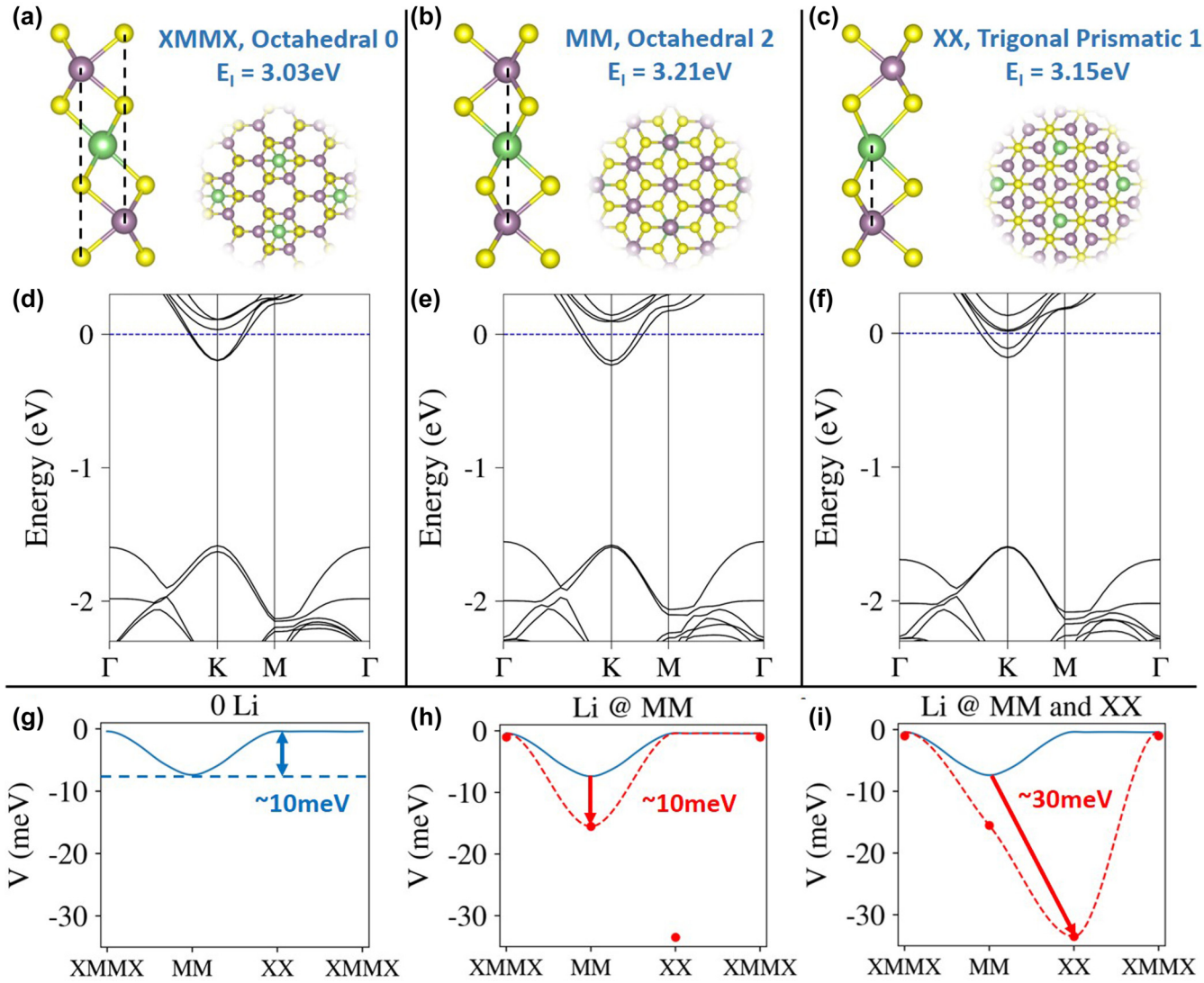

FIG. 5. Effects of Li on the moiré potential in $2H$-bilayer MoS_2. (a)–(c) Configurations with the most favorable intercalation energy (E_I): Li in the XMMX, MM, and XX regions with an intercalation density of one lithium per 2×2 supercell. (d)–(f) Band structures corresponding to the configurations shown in (a)–(c). (g)–(i) Approximate real space distribution of the interlayer moiré potential along the diagonal direction of the moiré supercell. From left to right: Without lithium, with lithium only in the MM region, and with lithium in both the MM and XX region.

appearance of flat bands, but such a term can play an important role in the complete model.

The interlayer interaction $V(\boldsymbol{r})$ acts like a potential energy for the electronic states in the moiré supercell, so we refer to it as the interlayer moiré potential. From the variation in this potential throughout the moiré supercell, we can obtain the band structure for the twisted bilayer. The potential $V(\boldsymbol{r})$ across the entire moiré supercell can be estimated from its value at the three high-symmetry stacking arrangements. The magnitude of $V(\boldsymbol{r})$ is simply one-half of the energy splitting of the lowest two states at the K conduction band edge (Fig. 5), while its phase is determined by details of the atomic geometry. Because the conduction band edge has primarily d orbital character, $V(\boldsymbol{r})$ is largest in the nonintercalated case when the metal atoms are aligned (MM configuration). Taking the MM stacking to correspond to $\boldsymbol{r} = 0$ and expanding the interlayer potential in the lowest harmonics of the reciprocal lattice vectors for the moiré supercell $\boldsymbol{G}_i^{sc}$ gives [3,17]

$$V(\boldsymbol{r}) = \frac{V_0}{3}\left(1 + e^{-i\boldsymbol{G}_1^{sc}\cdot\boldsymbol{r}} + e^{-i\boldsymbol{G}_2^{sc}\cdot\boldsymbol{r}}\right). \tag{6}$$

Compared to the results of Wu *et al.* [17], who studied TMDC homobilayers in an aligned phase, our system is in the nonaligned $2H$ phase. Although this provides a different crystal symmetry, the expansion is still a good match in the unintercalated case, as the splitting of the conduction band edge at K mostly depends on the distance between the metal atoms and not the detailed symmetry of the crystal structure. This enters the $\boldsymbol{k}$-dependent Hamiltonian $H_{\boldsymbol{k}}$ as three interlayer momentum scattering terms of equal strength [3]. The prefactor above is chosen as $V_0/3$ such that $V(0) = V_0$. Note that at the other two high-symmetry stackings $\boldsymbol{r} = n(\boldsymbol{a}_1^{sc} + \boldsymbol{a}_2^{sc})/3$ for $n = 1, 2$, the function V is identically zero. Lying along the diagonal direction of the moiré supercell, these are the same

three local stacking regions which provide stable intercalation sites for lithium. The most stable intercalation site for each of these local configurations is shown in Figs. 5(a)–5(c), with the band structure for a uniform cell with that stacking configuration immediately below in Figs. 5(d)–5(f).

Combining the results for the band splitting in each different stacking configuration, we can assemble the moiré potentials shown in Figs. 5(g)–5(i). The blue line in all three panels shows the moiré potential along the diagonal direction of the moiré supercell in $2H$-bilayer MoS_2 without lithium intercalation. It has a potential well around the MM stacking configuration which can localize the electronic states and presumably lead to flat bands and correlated physics. However, the potential well is only ∼10 meV deep.

When Li is introduced between the layers it will first collect in regions of MM stacking because they offer the most energetically favorable intercalation sites. This deepens the moiré potential near the MM locations by a factor of 2 and makes flat bands and correlated interactions more likely. Further intercalation results in lithium accumulation in regions of XX stacking, deepening the moiré potential but also changing its shape. Moving the origin ($\boldsymbol{r} = 0$) of the moiré potential amounts to a gauge choice in the interlayer coupling that does not affect the moiré band structure in the continuum model [3]. However, the lowest harmonic approximation of $V(\boldsymbol{r})$ now fails as the values at MM and XMMX are not identical. Since we only aim to estimate the effect of lithium intercalation on the moiré band structure, we ignore this complication and treat the potential well as for the MM case. To calculate the moiré band structure more accurately, it is necessary to include higher harmonics in the interlayer potential. Obtaining these harmonics from DFT calculations requires band structures for additional Li intercalated geometries, which can be challenging to optimize for low-symmetry stacking configurations.

VI. EMERGING FLAT BANDS

The strong effect of lithium intercalation on the interlayer moiré potential is useful in enhancing the flat bands of a twisted TMDC bilayer. In Fig. 6 the band structure obtained from the continuum model for the K point conduction bands of twisted $2H$-bilayer MoS_2 are shown for two different twist angles (2°, 1°) and the three cases of Li intercalation (zero, Li only at MM, and Li at both MM and XX). To match the DFT band structure calculations the value of V_0 for three

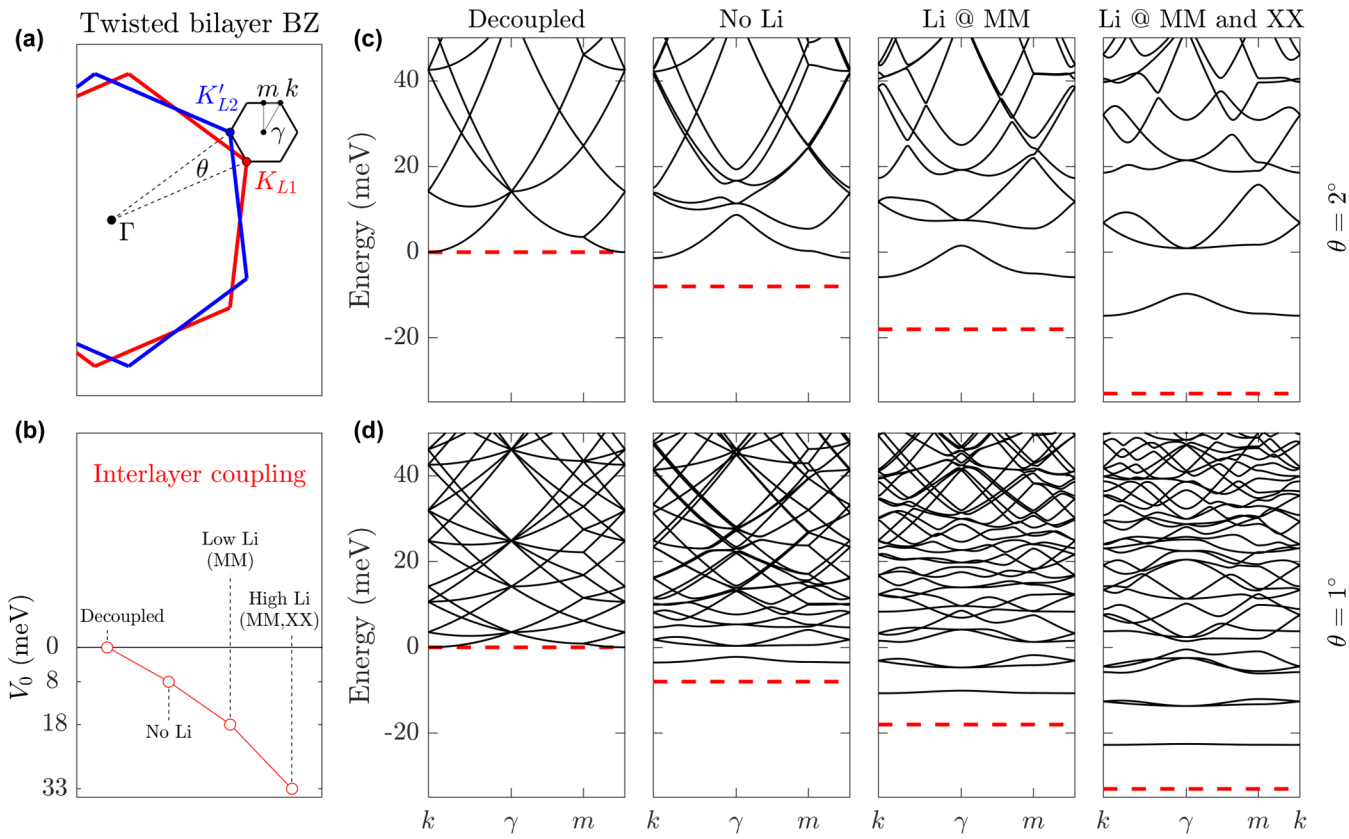

FIG. 6. Emerging flat bands in twisted $2H$-bilayer MoS_2 with lithium intercalation. (a) Brillouin zone (BZ) of the bottom layer (red) and top layer (blue) of a twisted $2H$-bilayer MoS_2. The moiré superlattice BZ is given in black, with its high-symmetry points in lowercase labels. (b) Dependence of the interlayer coupling strength on lithium intercalation in $2H$-bilayer MoS_2. A case with no interlayer coupling (decoupled) is included along with the three configurations of Li intercalants studied. The y axis is the same as for the band structures for ease of comparison. (c) and (d) Band structures of twisted $2H$-bilayer MoS_2 for θ equal to 2° and 1° using the continuum model. The interlayer coupling strength is varied by the details of lithium intercalation. The bands here are expanded from the conduction K valley, which is most relevant because of electron doping by the Li intercalants. The band edge of the monolayer conduction band is taken as 0 energy and the dashed red line shows the maximum depth of the interlayer-coupling potential in each case.

lithium intercalation cases is taken to be 8, 18, and 33 meV, respectively. The effective mass for the conduction band edge at K is obtained by fitting to the monolayer band structure, yielding $m^*/\hbar = 75\ \mathrm{meV}^{-1}\ \mathrm{Å}^{-2}$.

For a 2° twist angle, the unintercalated bilayer does not have a splitting between the lowest two superlattice bands, and is thus very far from flat-band behavior. With Li intercalation the strength of the moiré potential can be increased by a factor of 4, allowing flat bands to emerge even at this large twist angle. The 1° system has flat bands visible even at zero intercalation, but the intercalation greatly increases the gap between the superlattice bands and flattens the bands further. As Li concentration increases, not only does the lowest conduction band become flatter, but the bottom of the moiré potential well shifts from the regions of MM stacking to regions with XX stacking. As the moiré flat bands host large "spots" of electronic density confined by this potential well, a shifting of the electron density from MM stacking to XX stacking would be visible, for instance, in scanning tunneling microscopy.

Finally, we briefly discuss the effects of spin-orbit coupling on the conduction band continuum model. The states at the K conduction band are spin polarized, and we find there is negligible interspin coupling between the layers. Thus the two spins can be modeled as separate Hamiltonians, H_{up} and H_{down}, which depend on the spin splitting $\Delta_s \approx 3$ meV. We assume for the following discussion that the spin-orbit coupling is not enhanced by the band flattening. Although it is possible such an enhancement may occur, we note that it would not arise from the spin-orbit effect of the d-shell Mo electrons directly but rather from the orbits of the moiré quasiparticles within the twisted superlattice. For aligned (R) stacking, the two layers' band structures are identical and thus one can expect two nearly identical copies of the continuum model to exist: One for spin-up and one for spin-down. At a given valley, one of the spin channels will be 3 meV higher than the other, with the opposite spin channel higher at the opposite valley, e.g., $H_{\mathrm{up}} = H_{\mathrm{down}} \pm \Delta_s$. For 2$H$ stacking, in a given valley the spin-orbit splitting for the top layer will have the opposite sign compared to that of the bottom layer [17]. Instead of having an absolute shift between the up and down spin Hamiltonians, within a single spin channel the top and bottom layer are instead shifted by Δ_s relative to one another. Compared to the features of the band structures in Fig. 6 this is a small effect, but as the band energy at the K points of the two layers will differ by Δ_s we expect that the minimum bandwidth for the flat bands will be limited by Δ_s.

VII. CONCLUSION

We have performed first-principles DFT calculations and *ab initio* tight-binding and continuum modeling to explore the structural and electronic properties of lithium intercalation in twisted bilayer MoS_2 systems. We found that lithium intercalants have the lowest energy in MM and XX stacking regions in the moiré supercell. The presence of Li dramatically enhances the interlayer interaction, increasing the depth of the effective moiré potential well from ∼8 to ∼20 meV for Li in MM regions, and further to ∼33 meV for Li in XX stacking regions. Using a continuum model with an interlayer interaction based on these DFT results, we show that lithium intercalation can better flatten and isolate the conduction bands near the Fermi level. Furthermore, such moiré flat bands can be realized at larger twist angles with the aid of intercalation. Our results demonstrate that intercalation can be a powerful tool for controlling moiré flat bands in twistronic devices.

ACKNOWLEDGMENTS

We acknowledge Yiqi Xie, D. Kwabena Bediako, Mehdi Rezaee, and Tamar Mentzel for helpful discussions. The computations in this paper were run on the FASRC Odyssey cluster supported by the FAS Division of Science Research Computing Group at Harvard University. S.C. was supported by ARO MURI Award No. W911NF-14-0247 and by the STC Center for Integrated Quantum Materials, NSF Grant No. DMR-1231319.

[1] Y. Cao, V. Fatemi, A. Demir, S. Fang, S. L. Tomarken, J. Y. Luo, J. D. Sanchez-Yamagishi, K. Watanabe, T. Taniguchi, E. Kaxiras *et al.*, Correlated insulator behaviour at half-filling in magic-angle graphene superlattices, Nature (London) **556**, 80 (2018).

[2] Y. Cao, V. Fatemi, S. Fang, K. Watanabe, T. Taniguchi, E. Kaxiras, and P. Jarillo-Herrero, Unconventional superconductivity in magic-angle graphene superlattices, Nature (London) **556**, 43 (2018).

[3] R. Bistritzer and A. H. MacDonald, Moiré bands in twisted double-layer graphene, Proc. Natl. Acad. Sci. USA **108**, 12233 (2011).

[4] G. Chen, L. Jiang, S. Wu, B. Lyu, H. Li, B. L. Chittari, K. Watanabe, T. Taniguchi, Z. Shi, J. Jung *et al.*, Evidence of a gate-tunable Mott insulator in a trilayer graphene moiré superlattice, Nat. Phys. **15**, 237 (2019).

[5] G. Chen, A. L. Sharpe, P. Gallagher, I. T. Rosen, E. J. Fox, L. Jiang, B. Lyu, H. Li, K. Watanabe, T. Taniguchi *et al.*, Signatures of tunable superconductivity in a trilayer graphene moiré superlattice, Nature (London) **572**, 215 (2019).

[6] C. Shen, Y. Chu, Q. S. Wu, N. Li, S. Wang, Y. Zhao, J. Tang, J. Liu, J. Tian, K. Watanabe, T. Taniguchi, R. Yang, Z. Y. Meng, D. Shi, O. V. Yazyev, and G. Zhang, Correlated states in twisted double bilayer graphene, Nat. Phys. **16**, 520 (2020).

[7] Y. Cao, D. Rodan-Legrain, O. Rubies-Bigordà, J. M. Park, K. Watanabe, T. Taniguchi, and P. Jarillo-Herrero, Tunable correlated states and spin-polarized phases in twisted bilayer-bilayer graphene, Nature **583**, 215 (2020).

[8] X. Liu, Z. Hao, E. Khalaf, J. Y. Lee, K. Watanabe, T. Taniguchi, A. Vishwanath, and P. Kim, Tunable spin-polarized correlated states in twisted double bilayer graphene, Nature (London) **583**, 221 (2020).

[9] N. R. Chebrolu, B. L. Chittari, and J. Jung, Flat bands in twisted double bilayer graphene, Phys. Rev. B **99**, 235417 (2019).

[10] M. Koshino, Band structure and topological properties of twisted double bilayer graphene, Phys. Rev. B **99**, 235406 (2019).

[11] J. Y. Lee, E. Khalaf, S. Liu, X. Liu, Z. Hao, P. Kim, and A. Vishwanath, Theory of correlated insulating behaviour and spin-triplet superconductivity in twisted double bilayer graphene, Nat. Commun. **10**, 5333 (2019).

[12] C. Jin, E. C. Regan, A. Yan, M. I. B. Utama, D. Wang, S. Zhao, Y. Qin, S. Yang, Z. Zheng, S. Shi *et al.*, Observation of moiré excitons in WSe_2/WS_2 heterostructure superlattices, Nature (London) **567**, 76 (2019).

[13] K. L. Seyler, P. Rivera, H. Yu, N. P. Wilson, E. L. Ray, D. G. Mandrus, J. Yan, W. Yao, and X. Xu, Signatures of moiré-trapped valley excitons in $MoSe_2/WSe_2$ heterobilayers, Nature (London) **567**, 66 (2019).

[14] K. Tran, G. Moody, F. Wu, X. Lu, J. Choi, K. Kim, A. Rai, D. A. Sanchez, J. Quan, A. Singh *et al.*, Evidence for moiré excitons in van der Waals heterostructures, Nature (London) **567**, 71 (2019).

[15] E. M. Alexeev, D. A. Ruiz-Tijerina, M. Danovich, M. J. Hamer, D. J. Terry, P. K. Nayak, S. Ahn, S. Pak, J. Lee, J. I. Sohn *et al.*, Resonantly hybridized excitons in moiré superlattices in van der Waals heterostructures, Nature (London) **567**, 81 (2019).

[16] F. Wu, T. Lovorn, E. Tutuc, and A. H. MacDonald, Hubbard Model Physics in Transition Metal Dichalcogenide Moiré Bands, Phys. Rev. Lett. **121**, 026402 (2018).

[17] F. Wu, T. Lovorn, E. Tutuc, I. Martin, and A. H. MacDonald, Topological Insulators in Twisted Transition Metal Dichalcogenide Homobilayers, Phys. Rev. Lett. **122**, 086402 (2019).

[18] M. H. Naik and M. Jain, Ultraflatbands and Shear Solitons in Moiré Patterns of Twisted Bilayer Transition Metal Dichalcogenides, Phys. Rev. Lett. **121**, 266401 (2018).

[19] S. Carr, D. Massatt, M. Luskin, and E. Kaxiras, Duality between atomic configurations and Bloch states in twisted 2D bilayers, Phys. Rev. Research **2**, 033162 (2020).

[20] L. Wang, E.-M. Shih, A. Ghiotto, L. Xian, D. A. Rhodes, C. Tan, M. Claassen, D. M. Kennes, Y. Bai, B. Kim, K. Watanabe, T. Taniguchi, X. Zhu, J. Hone, A. Rubio, A. Pasupathy, and C. R. Dean, Magic continuum in twisted bilayer WSe_2, arXiv:1910.12147.

[21] M. Yankowitz, S. Chen, H. Polshyn, Y. Zhang, K. Watanabe, T. Taniguchi, D. Graf, A. F. Young, and C. R. Dean, Tuning superconductivity in twisted bilayer graphene, Science **363**, 1059 (2019).

[22] S. Carr, S. Fang, P. Jarillo-Herrero, and E. Kaxiras, Pressure dependence of the magic twist angle in graphene superlattices, Phys. Rev. B **98**, 085144 (2018).

[23] B. L. Chittari, N. Leconte, S. Javvaji, and J. Jung, Pressure induced compression of flatbands in twisted bilayer graphene, Electron. Struct. **1**, 015001 (2018).

[24] Z. Bi, N. F. Q. Yuan, and L. Fu, Designing flat bands by strain, Phys. Rev. B **100**, 035448 (2019).

[25] D. K. Bediako, M. Rezaee, H. Yoo, D. T. Larson, S. Y. F. Zhao, T. Taniguchi, K. Watanabe, T. L. Brower-Thomas, E. Kaxiras, and P. Kim, Heterointerface effects in the electrointercalation of van der Waals heterostructures, Nature (London) **558**, 425 (2018).

[26] D. T. Larson, I. Fampiou, G. Kim, and E. Kaxiras, Lithium intercalation in graphene–MoS_2 heterostructures, J. Phys. Chem. C **122**, 24535 (2018).

[27] D. T. Larson, S. Carr, G. A. Tritsaris, and E. Kaxiras, Effects of lithium intercalation in twisted bilayer graphene, Phys. Rev. B **101**, 075407 (2020).

[28] J. Xia, J. Wang, D. Chao, Z. Chen, Z. Liu, J.-L. Kuo, J. Yan, and Z. X. Shen, Phase evolution of lithium intercalation dynamics in 2H-MoS_2, Nanoscale **9**, 7533 (2017).

[29] C. Papageorgopoulos and W. Jaegermann, Li intercalation across and along the van der Waals surfaces of MoS_2 (0001), Surf. Sci. **338**, 83 (1995).

[30] G. Kresse and J. Furthmüller, Efficient iterative schemes for *ab initio* total-energy calculations using a plane-wave basis set, Phys. Rev. B **54**, 11169 (1996).

[31] G. Kresse and J. Furthmüller, Efficiency of ab-initio total energy calculations for metals and semiconductors using a plane-wave basis set, Comput. Mater. Sci. **6**, 15 (1996).

[32] J. Sun, A. Ruzsinszky, and J. P. Perdew, Strongly Constrained and Appropriately Normed Semilocal Density Functional, Phys. Rev. Lett. **115**, 036402 (2015).

[33] H. Peng, Z.-H. Yang, J. P. Perdew, and J. Sun, Versatile van der Waals Density Functional Based on a Meta-Generalized Gradient Approximation, Phys. Rev. X **6**, 041005 (2016).

[34] N. Marzari, A. A. Mostofi, J. R. Yates, I. Souza, and D. Vanderbilt, Maximally localized Wannier functions: Theory and applications, Rev. Mod. Phys. **84**, 1419 (2012).

[35] A. A. Mostofi, J. R. Yates, Y.-S. Lee, I. Souza, D. Vanderbilt, and N. Marzari, WANNIER90: A tool for obtaining maximally-localised Wannier functions, Comput. Phys. Commun. **178**, 685 (2008).

[36] G. Pizzi, V. Vitale, R. Arita, S. Blügel, F. Freimuth, G. Géranton, M. Gibertini, D. Gresch, C. Johnson, T. Koretsune, J. Ibañez-Azpiroz, H. Lee, J.-M. Lihm, D. Marchand, A. Marrazzo, Y. Mokrousov, J. I. Mustafa, Y. Nohara, Y. Nomura, L. Paulatto *et al.*, WANNIER90 as a community code: New features and applications, J. Phys.: Condens. Matter **32**, 165902 (2020).

[37] S. Fang, R. Kuate Defo, S. N. Shirodkar, S. Lieu, G. A. Tritsaris, and E. Kaxiras, *Ab initio* tight-binding Hamiltonian for transition metal dichalcogenides, Phys. Rev. B **92**, 205108 (2015).

[38] M. Chhowalla, D. Jena, and H. Zhang, Two-dimensional semiconductors for transistors, Nat. Rev. Mater. **1**, 16052 (2016).

[39] J. Yang, H. Kawai, C. P. Y. Wong, and K. E. J. Goh, Electrical doping effect of vacancies on monolayer MoS_2, J. Phys. Chem. C **123**, 2933 (2019).

[40] S. N. Shirodkar and E. Kaxiras, Li intercalation at graphene/hexagonal boron nitride interfaces, Phys. Rev. B **93**, 245438 (2016).

[41] J. C. Slater and G. F. Koster, Simplified LCAO method for the periodic potential problem, Phys. Rev. **94**, 1498 (1954).

[42] J. Jung, A. Raoux, Z. Qiao, and A. H. MacDonald, *Ab initio* theory of moiré superlattice bands in layered two-dimensional materials, Phys. Rev. B **89**, 205414 (2014).